J. Fluid Mech. (2011), *vol.* 672, *pp.* 109–129.
doi:10.1017/S0022112010005896

On the flow of buoyant fluid injected into a confined, inclined aquifer

IAIN GUNN AND ANDREW W. WOODS†

BP Institute for Multiphase Flow, University of Cambridge,
Madingley Road, Cambridge CB3 0EZ, UK

(Received 31 December 2009; revised 29 October 2010; accepted 9 November 2010;
first published online 15 February 2011)

We study the dispersal of a plume of incompressible buoyant fluid injected into a confined sloping aquifer which has an outflow at a single fault which may be up-dip (up-slope) or down-dip (down-slope) from the point of injection. We develop a long-time asymptotic solution for the motion of the injected fluid. We show that for the case in which the outflow fault is up-dip from the point of injection, there is a critical injection rate above which the injected fluid floods the full depth of the aquifer, and we show that for the case in which the outflow fault is down-dip from the point of injection, there is a critical injection rate below which all injected fluid initially flows up-dip. Our analysis leads to expressions for the lateral extent of the injected fluid as a function of time, and we consider the implications of the model for the dispersal of supercritical carbon dioxide injected into deep saline aquifers. The work also indicates that the geometry of the system may have a significant effect on (i) the total volume of carbon dioxide which it is possible to sequester in a faulted aquifer and (ii) the interpretation of the dispersed position of any injected tracers.

Key words: convection in porous media, gravity currents, Hele–Shaw flows

1. Introduction

There is growing interest in the process of carbon dioxide capture and storage, also known as carbon sequestration, for its potential role in the mitigation of anthropogenic climate change. Numerous studies have been carried out to explore the physical processes which control the migration of plumes of carbon dioxide (CO_2) injected into aquifers (e.g. Pruess *et al.* 2003; Obi & Blunt 2006; Neufeld, Vella & Huppert 2009). One of the key objectives of such modelling is to quantify the mechanisms and time scales associated with the possible migration of CO_2 back to man's environment.

When CO_2 is injected into a deep saline aquifer, it has the form of a supercritical fluid which is much less dense and less viscous than the water it displaces (Pruess *et al.* 2003; IPCC 2005), and will therefore tend to flow along the upper boundary of the aquifer as a buoyant gravity current. Many studies have focused on such buoyancy-driven flow of CO_2 through subsurface aquifers bounded by impermeable or low-permeability layers (Hesse, Tchelepi & Orr 2006; Nordbotten & Celia 2006; Vella & Huppert 2006; Hesse, Orr & Tchelepi 2008; Neufeld & Huppert 2009). Following injection, the plumes of CO_2 which develop are strongly influenced by the geometry of the aquifer, including structural traps, by capillary trapping of CO_2 at the

† Email address for correspondence: andy@bpi.cam.ac.uk

tail of the flow (Juanes *et al.* 2006), and by the dissolution of CO_2 into the formation water as the advancing plume displaces this water (Lyle, Huppert & Hallworth 2005; Nordbotten & Celia 2006; Bickle *et al.* 2007; Hesse *et al.* 2008; Farcas & Woods 2009). Trapped CO_2 may then gradually react with the rock matrix to become geologically sequestered (IPCC 2005).

However, if there are any pre-existing wells in the subsurface, or indeed if the casing or cement around any injection well fails, then these may act as conduits for the buoyant CO_2 to rise upwards through the geological strata, increasing the risk that some CO_2 returns to man's environment (Nordbotten, Celia & Bachu 2004; Nordbotten *et al.* 2005, 2009). Somewhat analogously, if the seal rock bounding an aquifer becomes fractured, it may allow some of the injected CO_2 to migrate upwards through the geological strata (Pritchard, Woods & Hogg 2001), leading to both vertical and lateral transport of the CO_2 plume. Since water and CO_2 are partially miscible, some of the CO_2 may still be trapped at depth (Hesse *et al.* 2008), but the remainder may be able to rise through the fracture system, towards the surface (Pritchard 2007; Farcas & Woods 2009; Woods & Farcas 2009).

If the aquifer is of relatively large vertical extent compared with the depth of the CO_2 current, the motion of the original fluid in the aquifer is of secondary importance to the flow (Barenblatt 1996; Hesse *et al.* 2008). In general, however, as the injected CO_2 displaces the original formation water, a two-layer flow results (Mitchell & Woods 2006; Nordbotten & Celia 2006; Hesse *et al.* 2008). In such a case, the aquifer is said to be 'confined'.

The fluid displaced by CO_2 injected into a confined aquifer may spread into the far field, eventually being accommodated by some large-scale deformation of the aquifer and confining rock (Class *et al.* 2009; Gasda, Nordbotten & Celia 2009), or it may be driven out of the aquifer through faults, rising to regions higher in the geological strata. If the flow is driven from the aquifer through a fault, two situations may exist depending on whether the fault is located up-dip or down-dip of the injection well (figure 1). These situations form the topic of this paper. The two most similar recent studies are Hesse *et al.* (2008), who consider an instantaneous finite release of buoyant fluid in the same geometry as the present paper, and Nordbotten & Celia (2006), who consider a maintained flux of injected fluid for a horizontal confined aquifer in a radial geometry.

A governing equation for a sharp-interface displacement in a confined, inclined aquifer in a two-dimensional geometry is developed by Bear (1988, § 9.5.5), whose approach we follow closely. The governing equation (3.6) is precisely a non-dimensionalised form of equation (9.5.64) of Bear (1988) with constant flux, and our governing equations ((3.7), (4.3) and (4.4)) are similarly derived. In a confined aquifer with an open end either up-dip or down-dip (that is, either up-slope or down-slope) from the injection site, there will be a net flow towards the open boundary from the injection well, but only a zero-flux exchange flow in the closed side of the layer. The governing equations differ depending on whether or not there is a net flux.

The key contribution of the present paper lies in providing new analytical solutions for the late-time behaviour of these systems and recognising the importance of different flux conditions in the far field on the flow of the fluids. We will seek to identify a series of different flow regimes and their dependence on the dimensionless injection rate and on the viscosity ratio of the injected to the original fluid. We discuss the implications of the results for modelling the dispersal of buoyant plumes of low viscosity fluid injected into faulted deep saline aquifers.

We note that, for simplicity, our analysis assumes incompressible flow, following the original approach of Bear (1988), and more recently Hesse *et al.* (2008), Pritchard

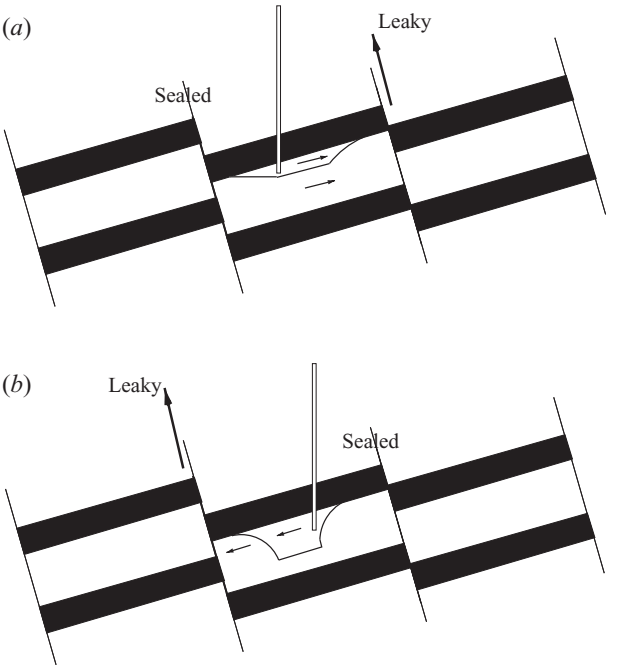

FIGURE 1. Diagram of the two modelled situations. (*a*) Confined aquifer with a permeable fault up-dip from the injection well. This situation is considered in § 3. (*b*) Confined aquifer with a permeable fault down-dip from the injection well. This situation is considered in § 4.

(2007) and Vella & Huppert (2006). We also neglect cross-slope motion, as is appropriate for a long horizontal well. The analysis is applicable for times after the current has spread far from the injection well, when the assumption that the flow is parallel to the base of the layer may therefore be applied. In the present work, we consider the evolution of the plume from such time as this assumption becomes valid until such time as the leading edge reaches a fault.

2. The model

We will briefly recount the development of a two-dimensional sharp-interface model for the flow of a buoyant fluid displacing an *in situ* fluid in a confined inclined aquifer, in a two-dimensional geometry, following Bear (1988, § 9.5). A discussion of the value of sharp-interface models for providing insight into key physics has been given by Woods & Norris (2010).

Consider the migration of a plume of buoyant fluid supplied from an injection well at the point $x = 0$ at a rate Q_I m^2 s^{-1} per unit distance cross-slope into a confined aquifer of depth H, lateral extent $L \gg H$ and inclination θ to the horizontal. We assume that the fluids are incompressible, that there is a sharp interface between the fluids, and that the motion is governed by Darcy's law.

The modelled layer is illustrated in figure 2. Note that x is the spatial coordinate in the up-dip direction, and z is the position above the base of the layer, measured perpendicularly to x (i.e. at an angle θ to the vertical). Let the buoyant current, occupying the region $h(x, t) < z < H$, have viscosity μ_1 and density ρ_1. Let the *in situ* fluid, occupying the region $0 < z < h(x, t)$, have viscosity μ_2 and density $\rho_2 = \rho_1 + \Delta\rho$. As the flow spreads laterally over a distance much greater than the thickness of the

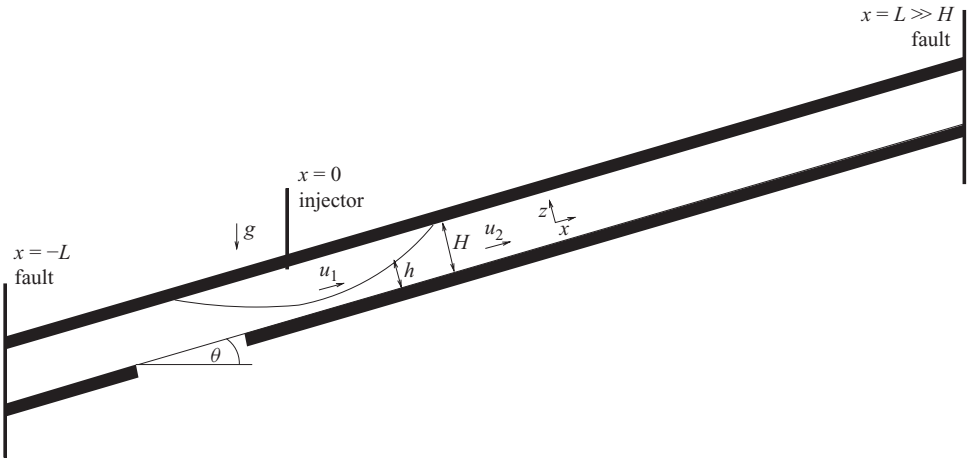

FIGURE 2. Diagram of the modelled layer.

layer, the pressure in the z-direction becomes approximately hydrostatic, with the flow being dominantly parallel to the upper and lower boundaries of the layer. Away from the point of injection and from the leaking fault, the pressure variation is therefore given by

$$p(x, z, t) = p_0(x, t) - \rho_2 g z \cos\theta \tag{2.1}$$

for $0 < z < h$, and

$$p(x, z, t) = p_0(x, t) - \Delta\rho g h \cos\theta - \rho_1 g z \cos\theta \tag{2.2}$$

for $z > h$, where $p_0(x, t)$ is the pressure on the lower boundary of the permeable layer. Darcy's law then leads to the relations

$$u_1 = -\frac{k}{\mu_1}\left(\frac{\partial p_0}{\partial x} - \Delta\rho g \cos\theta \frac{\partial h}{\partial x} + \rho_1 g \sin\theta\right), \tag{2.3}$$

$$u_2 = -\frac{k}{\mu_2}\left(\frac{\partial p_0}{\partial x} + \rho_2 g \sin\theta\right), \tag{2.4}$$

where u_1, u_2 are the transport velocities of the injectate and the *in situ* fluid, respectively, in the up-dip sense.

To complete the model for the flow, we require some conditions for mass conservation, and these depend on whether the permeable fault is located up-dip or down-dip from the injection point.

3. Permeable fault located up-dip from the injection well, in $x > 0$

In this section, we consider the case in which the up-dip fault is permeable, and all fluid displaced by the injected fluid escapes through this fault. The total flux up-dip from the injection point is then Q_I, while the net flux in the down-dip half-space is zero. Therefore, for an incompressible flow, by conservation of mass, in the region up-dip from the source $x > 0$,

$$Q_I = (H - h)u_1 + hu_2, \tag{3.1}$$

while in the region $x < 0$,

$$(H - h)u_1 + hu_2 = 0. \tag{3.2}$$

Finally, conservation of mass for the *in situ* fluid gives

$$\phi \frac{\partial h}{\partial t} = -\frac{\partial}{\partial x}(hu_2), \tag{3.3}$$

where ϕ is the porosity of the layer, presumed constant in space and time. By combining these equations and introducing the scalings

$$\tau = t/t_s = \frac{\Delta\rho g k \sin\theta}{\mu_1 \phi H} t, \quad \xi = \frac{x}{H}, \quad \hat{h} = \frac{h}{H}, \tag{3.4}$$

and the dimensionless parameters

$$V = \frac{\mu_1}{\mu_2}, \quad \Lambda = \frac{Q_I \mu_1}{\Delta\rho g k H \sin\theta}, \tag{3.5}$$

one finds that the current depth is given by the relation

$$\frac{\partial \hat{h}}{\partial \tau} = V \frac{\partial}{\partial \xi} \left(\frac{\hat{h}(1-\hat{h})\left(1 + \cot\theta \dfrac{\partial \hat{h}}{\partial \xi}\right) - \Lambda \hat{h}}{1 - \hat{h}(1-V)} \right) \tag{3.6}$$

for the region $x > 0$, and by

$$\frac{\partial \hat{h}}{\partial \tau} = V \frac{\partial}{\partial \xi} \left(\frac{\hat{h}(1-\hat{h})\left(1 + \cot\theta \dfrac{\partial \hat{h}}{\partial \xi}\right)}{1 - \hat{h}(1-V)} \right) \tag{3.7}$$

for $x < 0$.

The choice of scalings (3.4) has the advantage that $\phi\Lambda$ is the flux of the non-dimensionalised system:

$$\phi \Lambda = Q_I \frac{t_s}{H^2}. \tag{3.8}$$

This allows us to interpret Λ as a proxy for the injection flux Q_I. The other dimensionless parameter V is the ratio of the viscosity of the injected fluid to that of the *in situ* fluid (the inverse of the mobility ratio).

The parameter Λ may alternatively be interpreted as a densimetric Froude number, being the ratio of the speed associated with the injection flux Q_I/H to the x-component of the velocity associated with the buoyant slumping of the injected fluid, $\Delta\rho g k \sin\theta/\mu_1$. However, it should be noted that if a change in the value of Λ is considered to arise from a change in a dimensional parameter other than Q_I, there will be an associated change in the scaling of t. Thus, a direct comparison between results for different values of Λ is only informative if the different values of Λ are considered to be associated with different injection fluxes Q_I for an otherwise identical system.

Expanding (3.6) and (3.7), we obtain a pair of nonlinear advection–diffusion equations:

$$\frac{\partial \hat{h}}{\partial \tau} + f_{\pm}(\hat{h}) \frac{\partial \hat{h}}{\partial \xi} - V \cot\theta \frac{\partial}{\partial \xi} \left(\frac{\hat{h}(1-\hat{h})}{1 - \hat{h}(1-V)} \frac{\partial \hat{h}}{\partial \xi} \right) = 0, \tag{3.9}$$

where

$$f_+(\hat{h}) = -V\left(\frac{(1-V)\hat{h}^2 - 2\hat{h} + 1 - \Lambda}{(1-\hat{h}(1-V))^2}\right) \tag{3.10}$$

describes the advective behaviour for $\xi > 0$, and

$$f_-(\hat{h}) = -V\left(\frac{(1-V)\hat{h}^2 - 2\hat{h} + 1}{(1-\hat{h}(1-V))^2}\right) \tag{3.11}$$

describes the advective behaviour in $\xi < 0$.

The advection term $f_+(\hat{h})$ contains a component (Λ in the numerator of (3.10)) corresponding to flow driven by injection, and another component (the other terms in the numerator of (3.10)) corresponding to flow driven by the up-dip (x-axis) component of gravity. It is the advective term due to injection that distinguishes the governing equation for $\xi > 0$ from that for $\xi < 0$: the advection term $f_-(\hat{h})$ has an identical gravitational term to that in (3.10), but lacks the component due to injection, as there is no net flux in $\xi < 0$. The diffusion term in (3.9) corresponds to buoyant spreading of the injected fluid against the upper boundary, driven by the z-axis component of the gravitational force, and this is the same in $\xi > 0$ as in $\xi < 0$.

We can gain some insight into the expected behaviours of this system at long times by neglecting the diffusion term in (3.9), and considering the characteristics of the advection equations

$$\frac{\partial \hat{h}}{\partial \tau} + f_\pm(\hat{h})\frac{\partial \hat{h}}{\partial \xi} = 0. \tag{3.12}$$

The predictions made using this method will be compared with numerical integrations of the full governing equations (3.6) and (3.7) in § 3.1. Note, though, that at early times when $\cot\theta(\partial\hat{h}/\partial\xi) > 1$, the force due to the z-component of buoyancy is large compared with the other driving forces, and the flow will be controlled by the diffusive term, not by advection (cf. Huppert & Woods 1995).

Equations (3.12) have characteristic lines

$$\xi = f_\pm(\hat{h}_0)\tau. \tag{3.13}$$

Consider first the characteristics for the $\xi < 0$ half-space. Note that $f_-(\hat{h})$ is negative for $\hat{h} < [1/(1+\sqrt{V})]$, so one might conjecture that a shock arises propagating into the down-dip half-space. However, the total flux associated with this shock is

$$\text{flux} = -\phi\int_{\hat{h}_{base}}^{1} f_-(\hat{h})\,\mathrm{d}\hat{h} = -\phi V\frac{\hat{h}_{base}(1-\hat{h}_{base})}{1-\hat{h}_{base}(1-V)}, \tag{3.14}$$

which is zero for $\hat{h}_{base} = 0$ and negative for any higher value of $\hat{h}_{base}$, where the shock extends between $\hat{h}_{base}$ and 1. Therefore, the shock has zero or negative flux associated with it, and therefore no such shock propagates. Instead, we expect that there is no flux of injected fluid into the down-dip half-space, after the initial transient behaviour associated with the $\partial\hat{h}/\partial\xi$ term in (3.7), which establishes a static equilibrium in $\xi < 0$, given by the steady state solution of (3.7),

$$\frac{\mathrm{d}\hat{h}}{\mathrm{d}\xi} = -\tan\theta. \tag{3.15}$$

This equation describes a horizontal interface, as one would expect for a buoyant fluid overlying a denser fluid in a region of zero flow.

Consider now the characteristics for the $\xi > 0$ half-space. Note that $f_+(\hat{h})$ is positive for sufficiently large values of $\hat{h}$, so characteristics for these values of $\hat{h}$ will tend to propagate up-dip. The gradient of $f_+(\hat{h})$ is

$$f'_+(\hat{h}) = 2V\left(\frac{\Lambda(1-V)+V}{(1-\hat{h}(1-V))^3}\right). \tag{3.16}$$

This is always positive if $V < 1$ or if $\Lambda < [V/(V-1)]$. Therefore, if $V < 1$, or if $V > 1$ and Λ is sufficiently small, characteristics associated with higher values of $\hat{h}$ will tend to propagate up-dip faster than those with lower values of $\hat{h}$. For these cases, we may therefore expect a smooth front stretching into $\xi > 0$ with lateral extent in proportion to τ. Indeed, there is a closed-form similarity solution as a function of the variable $\eta = \xi/\tau$:

$$\hat{h} = \frac{1}{1-V}\left(1 - \sqrt{1 - \frac{\eta - V(\Lambda-1)}{\eta + \dfrac{V}{1-V}}}\right). \tag{3.17}$$

Equation (3.17) is an exact solution of the advection equation (3.12). The full governing equation (3.6) will tend to this solution as τ increases and the diffusion term becomes less important.

There are two possibilities for the range for which (3.17) is valid. If the injection flux is sufficiently large, then behind the similarity front, the injected fluid floods the layer from base $\hat{h} = 0$ to top $\hat{h} = 1$, and (3.17) then describes the front of this current at all heights $0 < \hat{h} < 1$. On the other hand, if there is insufficient flux of injected fluid to flood the entire height of the layer, then the current of injected fluid behind the front will flow only through heights $\hat{h}_p < \hat{h} < 1$ for some $\hat{h}_p > 0$, and (3.17) will hold only for those values of $\hat{h}$.

Now, the flux associated with all the characteristic curves for $\xi > 0$ above a given height $\hat{h}_p$ is given by

$$\text{flux} = \phi \int_{\hat{h}_p}^{1} f_+(\hat{h})\,\mathrm{d}\hat{h}. \tag{3.18}$$

By setting this flux equal to the total flux of injected fluid, $\phi\Lambda$, we can determine the depth $1 - \hat{h}_p$ taken by the current when the initial transient behaviour has concluded and all injected flux flows into $\xi > 0$. Setting the flux equal to $\phi\Lambda$ in (3.18) gives the condition

$$\hat{h}_p(1-\hat{h}_p) - \Lambda\hat{h}_p = 0, \tag{3.19}$$

and therefore either $\hat{h}_p = 1 - \Lambda$ or $\hat{h}_p = 0$. Hence, we expect that for slow injection rates $\Lambda < 1$, the injected fluid flows into the region $\xi > 0$ only above the height

$$\hat{h}_p = 1 - \Lambda. \tag{3.20}$$

There is then a region behind the similarity front in which the injected fluid flows as a current of constant depth $1 - \hat{h}_p = \Lambda$ parallel to the base of the layer, and the nose of this current is described by (3.17) for $\hat{h}_p < \hat{h} < 1$. On the other hand, if $\Lambda > 1$, we expect the injected fluid to flow into the region $\xi > 0$ at all heights from 0 to 1, completely flooding the layer. Equation (3.17) is then valid for all heights $0 < \hat{h} < 1$. In either of these two cases for which (3.17) describes the front of the current, the location of the leading edge of the current can be calculated by substituting $\hat{h} = 1$

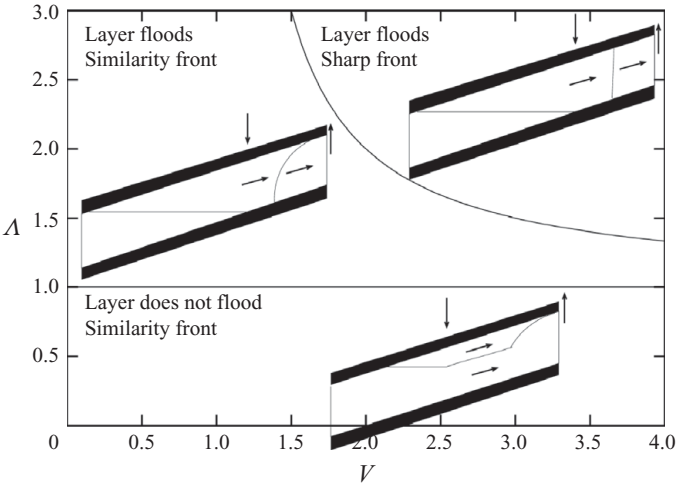

FIGURE 3. Above $\Lambda = 1$, the injected fluid floods the layer to its base. If the injected fluid is more viscous than the *in situ* fluid, then above $\Lambda = V/(V-1)$ a sharp front forms. Values of V relevant to CO_2 sequestration scenarios are approximately 0.05–0.25.

into (3.17), giving

$$\eta_{front} = 1 + \frac{\Lambda}{V}. \tag{3.21}$$

This speed is the speed of the characteristic associated with $\hat{h} = 1$, i.e. $f_+(1)$.

Consider now the case in which

$$V > 1 \quad \text{and} \quad \Lambda > \frac{V}{V-1}, \tag{3.22}$$

for which (3.17) is not a solution. In this case, (3.16) gives a negative value for $f'_+(\hat{h})$, so characteristics associated with smaller values of $\hat{h}$ will tend to propagate up-dip faster than characteristics associated with higher values of $\hat{h}$, and we would expect a shock front to form. Note, though, that the diffusion term in (3.9) which we have been neglecting would tend to smooth out the shock front somewhat; indeed, (3.9) admits a solution in the form of a steady travelling wave $\hat{h} \equiv \hat{h}(\zeta_+ \equiv \xi - \Lambda\tau)$ with constant gradient

$$\frac{\mathrm{d}\hat{h}}{\mathrm{d}\zeta_+} = \left(\Lambda - \frac{\Lambda}{V} - 1\right)\tan\theta, \tag{3.23}$$

which is finite. Note that in this regime (3.22), since $\Lambda > 1$, the flux of the injected fluid floods the layer, flowing at all heights. Therefore, at long times, volume conservation gives the asymptotic location of the front in the similarity coordinate as

$$\eta_{shock} = \Lambda, \tag{3.24}$$

cf. (3.21). The possible behaviours of the system as a function of the controlling parameters Λ and V are illustrated in the regime diagram figure 3.

The equation for the leading edge of the front (3.21) gives us insight into the dependence of the flow on the parameters Λ, V even within a given regime. For an injected fluid of smaller viscosity, corresponding to a smaller value of V, we expect the current to spread more rapidly along the upper boundary of the domain. The current depth at the source will have the same value ($1 - \hat{h}_p = \Lambda$ if we are in the

$\Lambda < 1$ regime), but the current will thin more rapidly for the case with the smaller value of V, so that total volume is conserved. In contrast, for a larger value of Λ, the current is deeper at the source and the nose advances more quickly – the current becomes both deeper and longer, because more fluid is being injected.

This result could have important implications for the fraction of the injected fluid which may ultimately be trapped by capillary retention in a layer once the injection has terminated, with less fluid being retained by capillary effects for a thinner current (cf. Hesse *et al.* 2008; Farcas & Woods 2009). Deeper sites for storage will have higher density and viscosity of CO_2, corresponding to higher values of Λ and V, and so these results suggest that plumes in such sites will form thicker currents with more CO_2 trapping, and which will take longer to break through to the leaking fault.

3.1. *Numerical calculations*

Our analytical predictions have been checked by numerical integration of the governing equations (3.6) and (3.7). The equations were integrated using a Crank–Nicolson scheme (Press *et al.* 1992), with the boundary condition at the injection well $\xi = 0$ being that the depth of the current is continuous,

$$h(0^+) = h(0^-). \tag{3.25}$$

Initially, the inflow is partitioned equally between the up-dip ($\xi > 0$) and down-dip ($\xi < 0$) half-spaces, as suggested by the limit of (3.6) and (3.7) at $t = 0$ and near the injection point $\xi = 0$. Subsequently, the partitioning of the injected flux between the up-dip and down-dip domains evolves in order to ensure that (3.25) is satisfied.

At each time step, a partitioning of Q_I into $Q_{up\text{-}dip}$ and $Q_{down\text{-}dip}$ is postulated. A value for $\hat{h}(0)$ is then calculated from the partitioning as follows. For the up-dip half-space, we combine

$$Q_{up\text{-}dip} = (H - h(0))u_1(0) \tag{3.26}$$

and

$$Q_I - Q_{up\text{-}dip} = h(0)u_2(0) \tag{3.27}$$

with (2.3) and (2.4) to give a boundary value for $\partial\hat{h}/\partial\xi$ as a function of the postulated values of $\hat{h}(0)$ and $Q_{up\text{-}dip}$. An equivalent condition is made for the down-dip half-space. An iterative relaxation method is used in each half-space to find a pair of values for $\hat{h}(0)$ and $\partial\hat{h}/\partial\xi$ for the next time step which satisfy (2.3), (2.4), (3.26) and (3.27) or the equivalent for the down-dip half-space. If the values of $\hat{h}(0)$ obtained by this process for each half-space agree within an error, this solution is taken as the solution for the next time step; if not, then a new partitioning is postulated by interval bisection and the process is repeated.

In this calculation, it is possible that points near the nose or base of the front overshoot $\hat{h} = 1$ or $\hat{h} = 0$, taking values $\hat{h} > 1$ or $\hat{h} < 0$. Therefore, after the solution for each new time step is calculated, we set the value of $\hat{h}$ to 1 or 0 respectively wherever it has taken a value greater than 1 or less than 0. This is the only special treatment given to the points $\hat{h} = 0$ and $\hat{h} = 1$; as expected from (3.23) and (4.23), we find in the numerics that the gradient of $\hat{h}$ does not become infinite at these points. We have tested our numerical results for robustness, finding that halving the space and time steps gives the same result, and in particular we have sufficient resolution to fully resolve the adjustment of the flow to zero depth at the nose.

Note that it is only through the boundary condition at the origin that the partitioning of the injected flux has an effect on the solution. The governing equations (3.6) and (3.7) have no dependence on the partitioning of the flux.

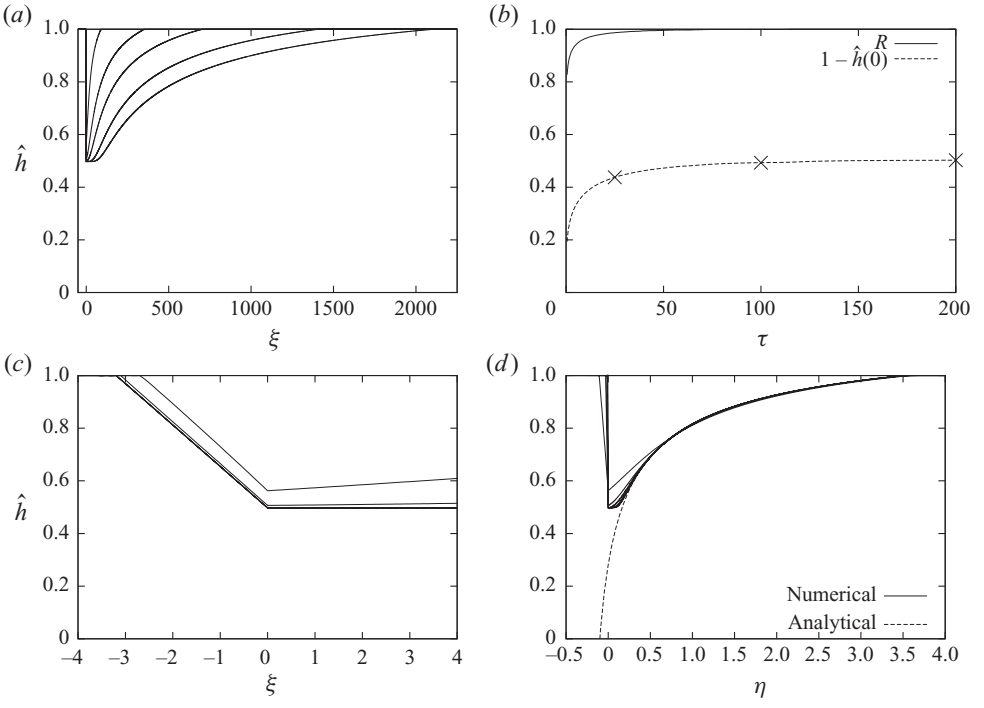

FIGURE 4. Evolution of an example current. In (a), we show variation of the current depth $\hat{h}$ as a function of the position ξ at times $\tau =$ 25, 100, 200, 400 and 600. Parameter values used are $\Lambda = 0.5$, $V = 0.2$ and $\theta = 9°$. Note the horizontal and vertical axes are of different scales. In (b), we show, as a function of the non-dimensionalised time τ, the fraction of the injected flux running upslope R (solid line) and the thickness of the current at the point of injection, $1 - \hat{h}(0)$ (dotted line marked with X at times corresponding to the first three profiles of a). (c) A detailed view of (a) in the region near the injection well, showing the adjustment to the steady-state horizontal interface in $\xi < 0$ and base-parallel interface in $\xi > 0$. Note that in (c), the profiles for times $\tau = 200$ and onwards are indistinguishable – the steady state has been reached to within the limits of numerical accuracy. (d) The profiles are shown as a function of the similarity variable η, with the solution (3.17) for comparison. Convergence to the similarity solution is rapid in the region towards the nose of the current, but slower towards the source. The development of the parallel-flow region behind the similarity front can be seen.

We now provide illustrative figures showing the numerical prediction of the evolution of an example current for each of the three regimes illustrated in figure 3. Our first example, figure 4, illustrates the case of slow injection, $\Lambda < 1$. Figure 4(a) shows the evolution of the depth of the current $\hat{h}$ as a function of position along the layer for the case $\Lambda = 0.5$, $V = 0.2$. As the current deepens, it also spreads both up-dip and down-dip. However, although the aspect ratio of the numerical plot is distorted (the horizontal scale is much greater than the vertical scale), we find that down-dip of the source, the interface becomes progressively more horizontal (see (3.15)). Figure 4(b) shows how the source flux is partitioned between the up-dip and down-dip components of the flow. The fraction of the flow which runs up-dip increases rapidly until all the flow runs up-dip, and the down-dip part of the current reaches an equilibrium shape. Eventually, the flow reaches the maximum depth $1 - \hat{h}_p = \Lambda$ at the source, and subsequently all the flow runs up-dip. The current then develops a growing region of constant depth up-dip from the source, with an adjustment zone to the leading edge of the current at $\hat{h} = 1$.

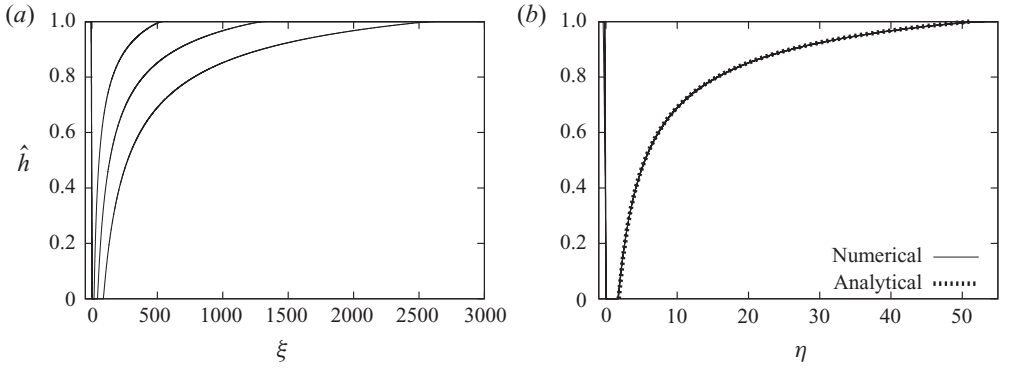

FIGURE 5. Evolution of the flow for the case $\Lambda = 10$, $V = 0.2$. Here $\hat{h}$ is plotted as a function of ξ (a) and the similarity variable η (b), for the times $\tau = 25$, 100 and 200. In (a), like figure 4(a), it is illustrated that down-dip of the point of injection, the injected fluid rapidly forms a stationary interface with the original fluid. The line in the region $\xi < 0$ corresponds to the horizontal interface on the down-dip side of the current. In (b), like figure 4(d), the convergence to the similarity solution (3.17) in $\xi > 0$ is illustrated.

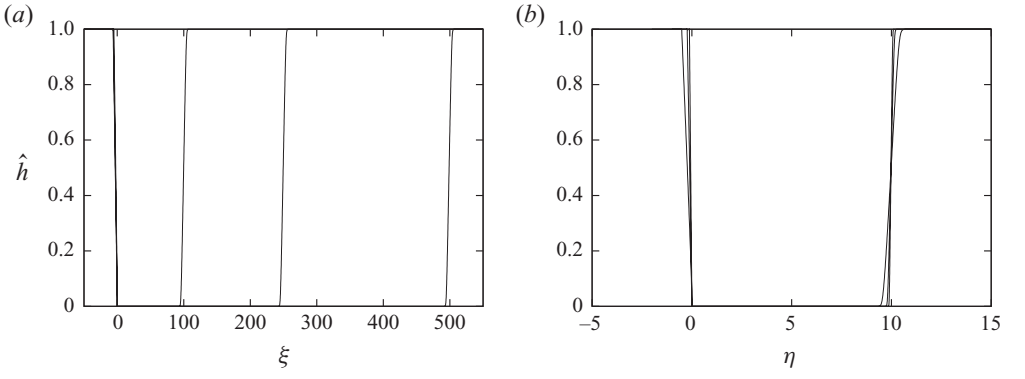

FIGURE 6. Evolution of the flow for the case $\Lambda = 10$, $V = 1.25$. Here $\hat{h}$ is plotted as a function of ξ (a) and the similarity variable η (b), for the times $\tau = 25$, 100 and 200, as for figure 5. In (a, b), we show the advancing front of constant gradient and the location of the front at $\eta = \Lambda$, respectively.

It now remains to provide illustrative numerical examples of the two types of current which may occur for fast injection rates, $\Lambda > 1$. When $\Lambda > 1$, the current deepens until it eventually makes contact with the lower boundary of the domain. Figure 5 illustrates the development of the current for the case $\Lambda = 10$, $V = 0.2$. In figure 5(a), it may be seen that up-dip from the injection point, the front of the current spreads and advances towards the permeable fracture; down-dip from the injection point, the interface between the fluids becomes horizontal (3.15). In figure 5(b), we have re-plotted these numerical solutions as a function of the variable $\eta = \xi/\tau$, and, as seen in figure 4(d) for the case $\Lambda < 1$, the numerical solution converges to the fixed profile (3.17), which now intersects both the upper and lower boundaries of the aquifer. Note that when $\Lambda > 1$, the position of the nose of the current is still given by (3.21), provided either $V < 1$ or $\Lambda < [V/(V-1)]$.

For completeness, we conclude this section by showing a case where $V > 1$ and $\Lambda > [V/(V-1)]$, and the flow is therefore viscosity-stabilised and piston-like, with a shock forming in the advection equation (3.12). Figure 6 shows the evolution of the

current for the case $\Lambda = 10$, $V = 1.25$. It should be noted that flows with $V > 1$ are not applicable to CO_2 sequestration scenarios.

4. Permeable fault located down-dip from the injection well, in $x < 0$

We now consider the complementary case in which all outflow from the layer occurs through a fault zone down-dip from the point of injection. In this case, it becomes possible for the flow to spread both up-dip, driven by the buoyancy forces, and down-dip towards the outflow fracture, driven by the applied pressure gradient from the injection well. The flow may be described using the same model as in § 3, but now the mass conservation equations become (cf. (3.1) and (3.2)):

$$(H-h)u_1 + hu_2 = 0, \qquad x > 0, \tag{4.1}$$

$$(H-h)u_1 + hu_2 = -Q_I, \qquad x < 0. \tag{4.2}$$

This results in the governing equations

$$\frac{\partial \hat{h}}{\partial \tau} = V\frac{\partial}{\partial \xi}\left(\frac{\hat{h}(1-\hat{h})\left(1+\cot\theta\dfrac{\partial \hat{h}}{\partial \xi}\right)}{1-\hat{h}(1-V)}\right) \tag{4.3}$$

in $\xi > 0$, and

$$\frac{\partial \hat{h}}{\partial \tau} = V\frac{\partial}{\partial \xi}\left(\frac{(1-\hat{h})\hat{h}\left(1+\cot\theta\dfrac{\partial \hat{h}}{\partial \xi}\right)+\Lambda\hat{h}}{1-\hat{h}(1-V)}\right) \tag{4.4}$$

in $\xi < 0$, where the same scalings have been used as in § 3 (see (3.4) and (3.5)). Note that (4.3) is identical to (3.7), and (4.4) is equivalent to (3.6) with the transformation $\Lambda \to -\Lambda$. Again, as in § 3, by expanding these equations we can express the model as a pair of nonlinear advection–diffusion equations:

$$\frac{\partial \hat{h}}{\partial \tau} + g_{\pm}(\hat{h})\frac{\partial \hat{h}}{\partial \xi} - V\cot\theta\frac{\partial}{\partial \xi}\left(\frac{\hat{h}(1-\hat{h})}{1-\hat{h}(1-V)}\frac{\partial \hat{h}}{\partial \xi}\right) = 0, \tag{4.5}$$

where

$$g_{+}(\hat{h}) = -V\left(\frac{(1-V)\hat{h}^2 - 2\hat{h} + 1}{(1-\hat{h}(1-V))^2}\right) \tag{4.6}$$

describes the advective behaviour in $\xi > 0$, and

$$g_{-}(\hat{h}) = -V\left(\frac{(1-V)\hat{h}^2 - 2\hat{h} + 1 + \Lambda}{(1-\hat{h}(1-V))^2}\right) \tag{4.7}$$

describes the advective behaviour in $\xi < 0$. As in § 3, we neglect the diffusion terms and attempt to gain insight into the system by considering the characteristics of the advection equations

$$\frac{\partial \hat{h}}{\partial \tau} + g_{\pm}(\hat{h})\frac{\partial \hat{h}}{\partial \xi} = 0. \tag{4.8}$$

As before, predictions made using this method will be compared with numerical integrations of the full governing equations (in this case (4.3) and (4.4)).

Equations (4.8) have characteristic lines

$$\xi = g_{\pm}(\hat{h}_0)\tau. \tag{4.9}$$

Let us consider first the characteristics for the $\xi > 0$ half-space. Note that $g_+(\hat{h})$ is positive for $h > [1/(1+\sqrt{V})]$, and

$$g'_+(\hat{h}) = \frac{2V^2}{(1-\hat{h}(1-V))^3} \tag{4.10}$$

is positive always. Therefore, characteristics associated with higher values of $\hat{h}$ are swept up-dip faster than those associated with lower values of $\hat{h}$, and we expect a smooth front stretching up-dip in proportion to τ. In contrast with the case in § 3, we do not expect to find a shock front for the up-dip flowing current, even if $V > 1$. Following § 3, we note that the nose of the flow ahead of the parallel flow region is described by a similarity solution (equivalent to (3.17)), with the form

$$\hat{h} = \frac{1}{1-V}\left(1 - \sqrt{1 - \frac{\eta + V}{\eta + \dfrac{V}{1-V}}}\right). \tag{4.11}$$

There are two possibilities for the range for which (4.11) is valid. If the injection flux is above a critical value, defined to be $\phi\Lambda_C$, then injectate flows into $\xi > 0$ at all heights $[1/(1+\sqrt{V})] < \hat{h} < 1$, and (4.11) then describes the flow everywhere from the origin $\xi = 0$ to the nose of the flow $\hat{h} = 1$. However, if the injection flux is not sufficiently large, $\phi\Lambda < \phi\Lambda_C$, then injectate flows into $\xi > 0$ only above some height $\hat{h}_{p+} > [1/(1+\sqrt{V})]$, and (4.11) then describes the flow only at the front of a current of constant depth $1 - \hat{h}_{p+}$. In contrast with the case for § 3, it is not possible for the injected fluid to flood the layer and flow at all heights $0 < \hat{h} < 1$, because $g_+(\hat{h})$ is negative for $\hat{h} < [1/(1+\sqrt{V})]$.

The flux associated with all up-dip propagating characteristics above height $\hat{h}_{p+}$ is given by

$$\text{flux} = \phi \int_{\hat{h}_{p+}}^{1} g_+(\hat{h})\,\mathrm{d}\hat{h}. \tag{4.12}$$

If all injected flux $\phi\Lambda$ flows up-dip, then by setting flux $= \phi\Lambda$ in this equation, we obtain the implicit expression for $\hat{h}_{p+}$,

$$\Lambda = \frac{V\hat{h}_{p+}(1-\hat{h}_{p+})}{1-\hat{h}_{p+}(1-V)}, \tag{4.13}$$

with explicit solution

$$\hat{h}_{p+} = \frac{1}{2}\left(1 - \frac{\Lambda}{V}(V-1) + \sqrt{\left(\frac{\Lambda}{V}(V-1) - 1\right)^2 - 4\frac{\Lambda}{V}}\right). \tag{4.14}$$

By equating (4.14) and (4.11), we can calculate the location $\eta = \eta_S$, at which the zone of uniform depth merges into the similarity solution associated with the nose region (i.e. the point where $\hat{h}(\eta) = \hat{h}_{p+}$), and calculate the critical value $\Lambda = \Lambda_C$ associated

with $\eta_S = 0$:

$$\Lambda_C = \frac{V}{(1+\sqrt{V})^2}. \tag{4.15}$$

The solution (4.11) identifies that the leading edge of the flow in $\xi > 0$, $\hat{h} = 1$, is located at

$$\eta_{front} = 1, \tag{4.16}$$

which is independent of both Λ and V, in contrast with the case in the previous section (3.21). Equation (4.16) is valid for all positive Λ and V.

In the case $\Lambda = \Lambda_C$, the solution for the up-dip flow follows the similarity solution (4.11) everywhere in $\eta > 0$. If $\Lambda > \Lambda_C$, the remaining fraction of the flow with flux $\phi(\Lambda - \Lambda_C)$ must flow into $\xi < 0$ and advance down-dip towards the outflow; we now consider this case. First, note that if the injected fluid is flowing into $\xi > 0$, then it cannot flow into $\xi < 0$ at all heights $0 < \hat{h} < 1$, because the *in situ* fluid which is displaced by the injected fluid in $\xi > 0$ also flows into the region $\xi < 0$. We therefore expect to find a current of constant depth $1 - \hat{h}_{p-} < 1$ in $\xi < 0$, with either a smooth decrease to zero depth at the nose or a shock front.

If the flux of injectate migrating into the region $\xi < 0$ is $\phi(\Lambda - \Lambda_C)$, then the height of the parallel constant-depth flow in $\xi < 0$ associated with that flux may be calculated as

$$\Lambda - \Lambda_C = -\int_{\hat{h}_{p-}}^{1} g_-(\hat{h})\,\mathrm{d}\hat{h}. \tag{4.17}$$

This gives the implicit expression

$$\frac{\Lambda_C}{V} = \frac{\hat{h}_{p-}(1-\hat{h}_{p-}) + \Lambda\hat{h}_{p-}}{1 - \hat{h}_{p-}(1-V)}, \tag{4.18}$$

which has explicit solution

$$\hat{h}_{p-} = \frac{1}{2}\left(\Lambda + 1 + \frac{1-V}{(1+\sqrt{V})^2} - \sqrt{\left(\Lambda + 1 + \frac{1-V}{(1+\sqrt{V})^2}\right)^2 - \frac{4}{(1+\sqrt{V})^2}}\right). \tag{4.19}$$

Figure 7 shows the variation of the depth of $\hat{h}_{p-}$ as a function of the viscosity ratio V for several values of Λ. As the viscosity of the injected fluid increases, the depth of the current of injected fluid migrating down-dip increases.

Let us now consider the front of the down-dip current. Note that

$$g'_-(\hat{h}) = -V\left(\frac{\Lambda(1-V) - V}{(1-\hat{h}(1-V))^3}\right), \tag{4.20}$$

and therefore for $V < 1$, $g'_-(\hat{h})$ is always negative if

$$\Lambda > \frac{V}{1-V} = \Lambda_N, \tag{4.21}$$

and always positive otherwise. Therefore, we expect a smooth similarity front in the down-dip direction if $\Lambda > \Lambda_N$, and a shock front otherwise. In fact, the advection equation for $\xi < 0$ admits a closed-form similarity solution in terms of the similarity

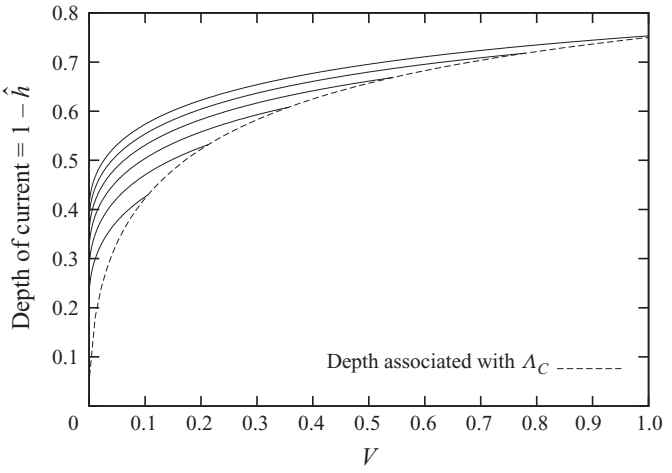

FIGURE 7. Depth $1-\hat{h}_{p-}$ of the parallel-flow part of the current down-dip of the point of injection as a function of V for the cases $\Lambda = 0.06, 0.1, 0.14, 0.18, 0.22$ and 0.26. Smaller values of Λ correspond to smaller depths. If $\Lambda > 0.25$ then $\Lambda > \Lambda_C$ for all V in $0 < V < 1$, but the curves for smaller values of Λ terminate at the dashed line, indicating the depth associated with $\Lambda_C(V)$.

variable $\eta = \xi/\tau$, given by

$$\hat{h} = \frac{1}{1-V}\left(1 - \sqrt{1 - \frac{\eta + V(1+\Lambda)}{\eta + \dfrac{V}{1-V}}}\right). \tag{4.22}$$

Requiring the solution to satisfy $(\partial\hat{h}/\partial\xi) < 0$, to describe the leading edge of the down-dip flow, leads to the recovery of the condition (4.21) for $V < 1$.

For the case $\Lambda_C < \Lambda < \Lambda_N$, where the advection equation has a shock solution, the full equation (4.4) has a steady-wave solution of the form $\hat{h} \equiv \hat{h}(\zeta_- \equiv \xi + \Lambda\tau)$ with constant gradient

$$\frac{\mathrm{d}\hat{h}}{\mathrm{d}\zeta_-} = \left(\frac{\Lambda}{V} - \Lambda - 1\right)\tan\theta, \tag{4.23}$$

which is finite. The possible behaviours of the system as determined by the controlling parameters Λ and V are illustrated in figure 8.

The model implies that injection of a low viscosity, buoyant fluid can produce a viscous fingering-type front in the down-dip direction (against buoyancy) if the injected fluid is injected sufficiently rapidly or has sufficiently small viscosity compared with the original formation fluid. The existence of the intermediate regime in which the descending front of the injected fluid is a sharp shock front (as in figure 10), which develops for small viscosity contrast or slow injection, is reminiscent of the buoyancy-controlled stabilisation of a descending front of buoyant but less viscous fluid when it moves with sufficiently low interface speed (see e.g. Phillips 1991, p. 163).

4.1. *Numerical calculations*

We have presented analytical calculations which predict three regimes for flow in the case of a down-dip leaking fault. These regimes, and the values of the controlling parameters giving rise to them, are illustrated in figure 8. For small values of Λ,

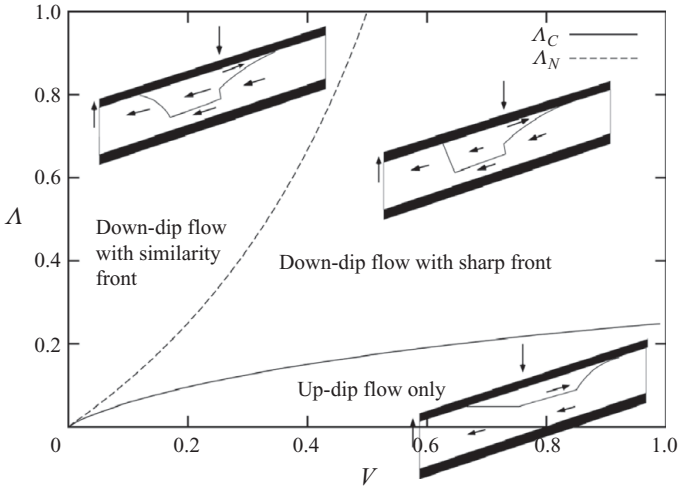

FIGURE 8. Maximum value of Λ for which all injected fluid flows up-dip Λ_C and the value of Λ above which a similarity front forms down-dip, Λ_N.

$\Lambda < \Lambda_C$, the injected fluid all tends to flow up-dip, the buoyancy effect being dominant. Behind the similarity front in $\xi > 0$, the injected fluid flows as a current of constant depth. For intermediate values of Λ, $\Lambda_C < \Lambda < \Lambda_N$, some injected fluid flows up-dip and some down-dip, with a sharp interface at the leading edge of the down-dip flow. Behind this sharp interface in $\xi < 0$, the injected fluid flows as a current of constant depth. For large values of Λ, $\Lambda > \Lambda_N$, injected fluid flows up-dip and down-dip, with a smooth adjustment of the current depth to zero at the advancing front of both currents. Behind the similarity solution in $\xi < 0$, the injected fluid flows as a current of constant depth. We will now provide illustrative figures showing the numerical evolution of an example current for each of these three regimes.

In the case of slow injection, although at early times the injected fluid spreads both up-dip and down-dip, it asymptotes to a flow in which all injected fluid migrates up-dip while a steady current profile develops in $\xi < 0$, given by the static solution of (4.4) with $\partial \hat{h}/\partial \tau = 0$. All flow down-dip then consists of the original formation fluid. In the region near the injection well, up-dip from the source, the flow has a region of constant depth, where the base of the current is parallel to the base of the layer, and the flow depth then adjusts to zero in a nose region ahead of this. Figure 9 shows the evolution of an example current in this regime.

If $\Lambda > \Lambda_C$, then more fluid is injected into the layer than can flow up-dip under buoyancy. The flow in $\xi > 0$ is everywhere described by the similarity solution (4.11) and the position of the nose of the flow in $\xi > 0$ is given by (4.16); there is no parallel-flow region in $\xi > 0$. The excess flux $\phi(\Lambda - \Lambda_C)$ flows down-dip, in a layer of constant depth. The evolution of an example current for the regime $\Lambda_C < \Lambda < \Lambda_N$ is shown in figure 10. The up-dip similarity solution is well established by time $\tau = 250$, although the down-dip current is still some way from establishing the constant-depth zone by that time.

The evolution of an example current in the regime $\Lambda > \Lambda_N$ is illustrated in figure 11. Further numerical calculations show that the depths of the parallel-flow regions of the three regimes agree very well with the analytical predictions (4.14) and (4.19).

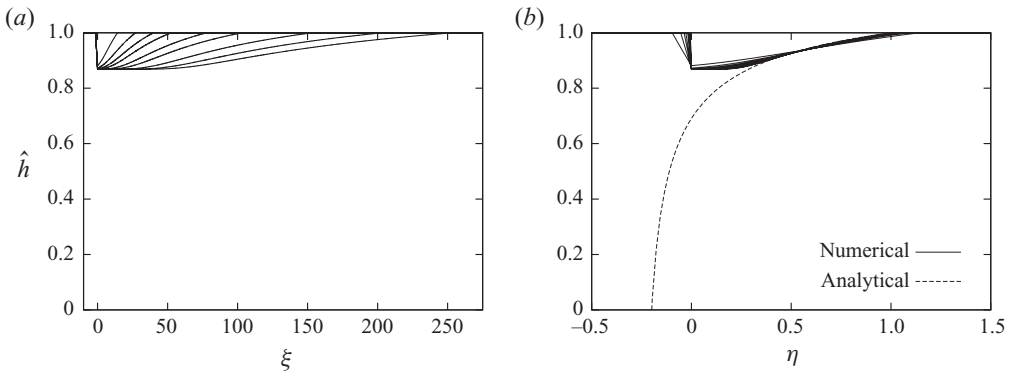

FIGURE 9. Evolution of the flow for the case $\Lambda = 0.075$, $V = 0.2$. Here $\hat{h}$ is plotted as a function of ξ (*a*) and the similarity variable η (*b*), for the times $\tau = 12.5, 25, 37.5, 50, 75, 100, 150, 200$ and 250. In (*a*), it is illustrated that down-dip of the point of injection, the injected fluid rapidly forms a stationary interface with the original fluid. In (*b*), the convergence to the similarity solution (4.11) of the leading edge of the up-dip current is shown, with a parallel-flow region behind the front.

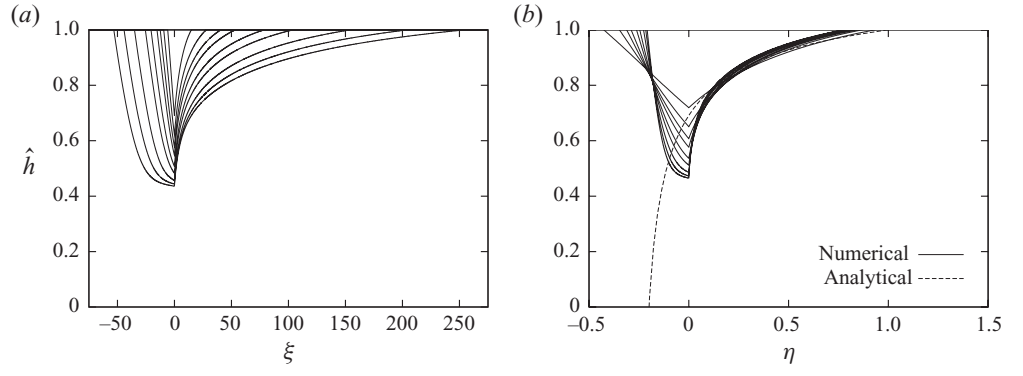

FIGURE 10. Evolution of the flow for the case $\Lambda = 0.2$, $V = 0.2$. Here $\hat{h}$ is plotted as a function of ξ (*a*) and the similarity variable η (*b*), for the times $\tau = 12.5, 25, 37.5, 50, 75, 100, 150, 200$ and 250. In (*b*), we illustrate the convergence to the similarity solution (4.11) in $x > 0$.

5. Discussion and application

We have analysed the motion of a maintained release of buoyant fluid as it spreads through a confined aquifer, noting that we have made a number of simplifying assumptions (in particular, we neglect compressibility). The modelling has identified some of the key controls on the motion of the current, including the roles of buoyancy, of the mobility ratio and of the rate of injection, an increase in any of which tends to accelerate the migration of the fluid along the layer. Depending on the location of the leaking fault, and on the values of the dimensionless controlling parameters Λ and V, the system will exhibit one of the six possible flow regimes illustrated in figure 12.

The analysis presented in this paper is important for describing currents for which $\Lambda < 10$; for values $\Lambda \gg 10$, the ratio of injection speed to the x-component of buoyancy is large, and the effects of slope are negligible, though fingering may still occur. Using the definition of Λ (3.5), one can easily calculate whether $\Lambda < 10$

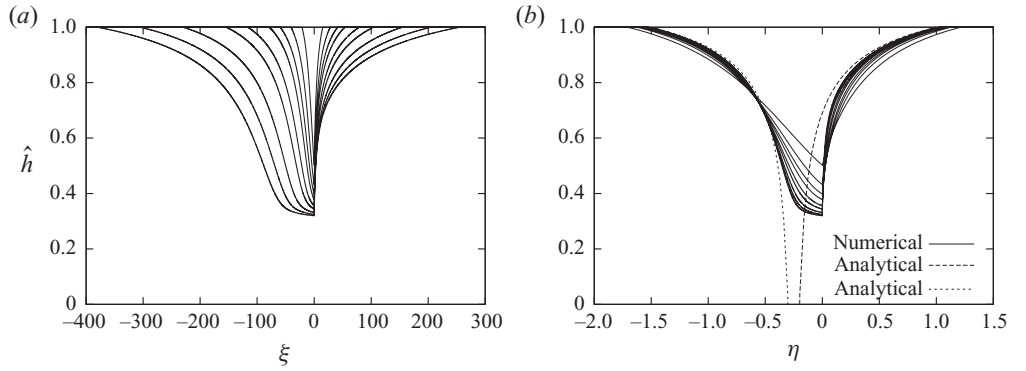

FIGURE 11. Evolution of the flow for the case $\Lambda = 0.5$, $V = 0.2$. Here $\hat{h}$ is plotted as a function of ξ (a) and the similarity variable η (b), for the times $\tau = 12.5, 25, 37.5, 50, 75, 100, 150, 200$ and 250. Profiles from earlier times are closer to the origin in (a), and may be distinguished as being less deep in $-0.5 < \eta < 0$ in (b), as convergence to parallel flow is slower than convergence to the similarity fronts. In (b), the convergence to the similarity solution (4.11) in $x > 0$ and the similarity solution (4.22) in $x < 0$ is shown.

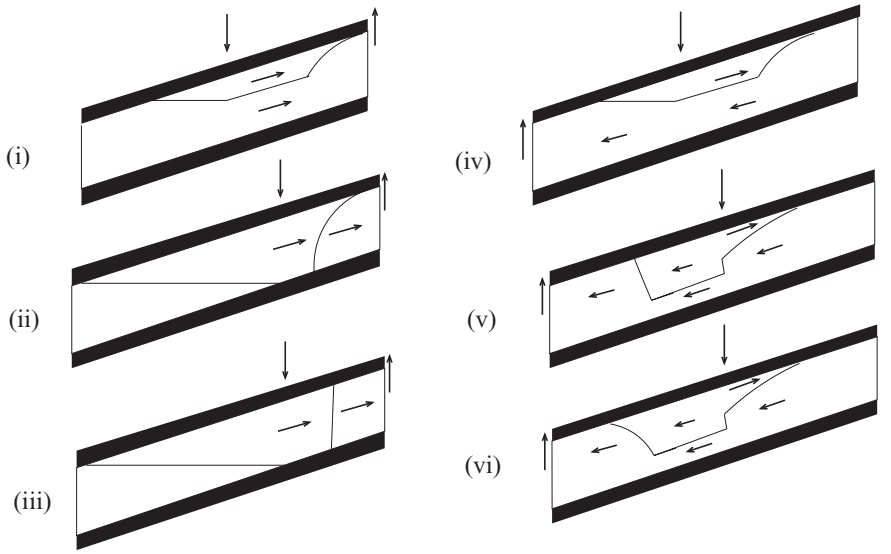

FIGURE 12. Possible flow regimes. Cases (i)–(iii) correspond to an injection well down-dip from the permeable fault, and the values of the controlling parameters for which each of these cases arises are illustrated in figure 3. Cases (iv)–(vi) correspond to an injection well up-dip from the permeable fault, and the values of the controlling parameters for which each of these cases arises are illustrated in figure 8. Cases (i) and (iv) correspond to lower injection rates and cases (ii), (iii), (vi) correspond to higher injection rates. Case (v) corresponds to an injection rate intermediate between that of case (iv) and case (vi). Case (iii) can occur only if the injected fluid is more viscous than the *in situ* fluid.

for a given layer. Let us consider what range of values of Λ may be physical: if the total injected flux, through a horizontal injection well 10^3 m long, is between 10^{-2} and 10^{-1} m^3 s^{-1} (IPCC 2005), an effective 2D injection flux of 10^{-5}–10^{-4} m^2 s^{-1} would develop. Taking viscosity to be $\sim 10^{-4}$ Pa s, permeability to be between 10^{-12} m^2 (as in the case of the Sleipner field, Bickle *et al.* 2007) and 10^{-14} m^2 (as in the case of

the In Salah reservoir, Cavanagh & Ringrose 2010), $\Delta\rho$ of the order of 10^2 kg m^{-3}, $g = 10$ m s^{-2}, 10 m $< H <$ 100 m and $0.01 < \sin\theta < 0.1$, we find that Λ may take values from 0.1 to 10^4, with the lower limit corresponding to high-permeability deep aquifers with a long horizontal well.

The case in which the permeable fault is down-dip from the injection point is particularly interesting. With low injection rates, injected CO_2 will initially flow up-dip, and may (after the current has reached the non-permeable up-dip fault) flood the layer up-dip. As a result, there may be a large spatial decorrelation between the location of the leak and the locations initially flooded by CO_2. Any tracers injected to monitor the flow may also initially spread a great distance from both the injection point and the leaking fault. The geometry of the system may have important implications for the total volume of the layer which it is possible to flood with CO_2, and hence the volume of water in the layer which is available for dissolution of the CO_2 (Bachu & Adams 2003), and also the mass of CO_2 which may be trapped in the layer as residual CO_2 following the injection phase (Juanes *et al.* 2006; Hesse *et al.* 2008).

Although the modelling in this paper is simplified, it has the benefit of producing analytical results with which the sensitivity of the flow to different parameters may be tested. A key result is our prediction of the location of the advancing nose of the current as a function of time. For the case of an up-dip permeable fault, putting (3.21) in dimensional terms, this is given by

$$x = \left(\frac{\Delta\rho g k \sin\theta}{\phi\mu_1} + \frac{\mu_2}{\mu_1}\frac{Q_I}{\phi H}\right)t = \frac{\Delta\rho g k \sin\theta}{\phi\mu_1}\left(1 + \frac{\Lambda}{V}\right)t, \tag{5.1}$$

where $\Lambda = Q_I\mu_1/\Delta\rho g k H \sin\theta$ and $V = \mu_1/\mu_2$, as defined in § 3. In contrast, in the case of a down-dip permeable fault, the position of the up-dip leading edge is, from (4.16),

$$x = \frac{\Delta\rho g k \sin\theta}{\phi\mu_1}t, \tag{5.2}$$

and if $\Lambda > \Lambda_C$ there is also a down-dip flow. These predictions are valid for times $t \gg (\mu_1\phi H/\Delta\rho g k \sin\theta)$.

We infer that, owing to the influence of the mobility ratio $1/V = \mu_2/\mu_1$, in the case of an up-dip leaking fault, the up-dip leading edge may advance considerably faster than in the case of a down-dip leaking fault. Figure 13 compares the speeds and distances travelled for example cases. The rates of advance of the leading edges are plotted in figure 13(*a*) as a function of permeability k for (i) the case of a down-dip leaking fault and (ii)–(iv) three example cases with an up-dip leaking fault. Figure 13(*a*) shows that for a given permeability, the flow runs up-dip more rapidly in the case of an up-dip leaking fault, as can be seen from (5.1) and (5.2). However, points A and B on the figure, which correspond to currents with the same up-dip speed, illustrate the potential challenge of interpreting measurements of the location of the nose of the flow, such as may be obtained, for example, from a seismic survey which is able to detect changes in the fluid within the rock (see e.g. Bickle *et al.* 2007). In particular, if a current is running up-dip with a given speed, the positions of points A and B on their respective curves show how this may be interpreted as either a low-permeability formation with an up-dip leaking fault, or a higher permeability formation with a down-dip leaking fault. As the speed of the nose increases, the difference between the permeabilities associated with these two interpretations decreases.

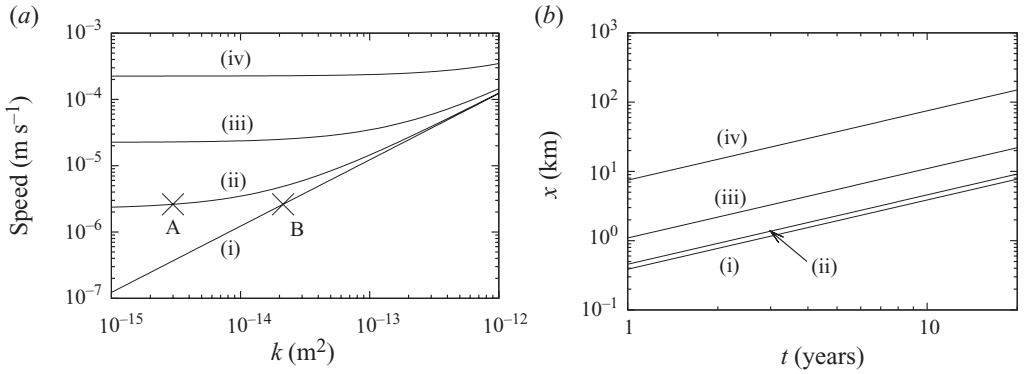

FIGURE 13. For four example cases: (*a*) shows the rate of advance of the up-dip front of the current as a function of permeability. For the same four cases, (*b*) shows the position of the nose of the up-dip current as a function of time, for the permeability $k = 1 \times 10^{-13}$ m^2. The four cases are: (i) a leaking down-dip fault; then the cases of a leaking up-dip fault for values (ii) $Q = 10^{-6}$ m^2 s^{-1}, $H = 100$ m; (iii) $Q = 10^{-6}$ m^2 s^{-1}, $H = 10$ m; and (iv) $Q = 10^{-5}$ m^2 s^{-1}, $H = 10$ m. Parameter values used are $\mu_1 = 2 \times 10^{-5}$ Pa s, $\mu_2 = 9 \times 10^{-4}$ Pa s, $\Delta\rho = 250$ kg m^{-3}, $g = 9.81$ m s^{-2}, $\sin\theta = 0.2$, $\phi = 0.2$.

More generally, the results of the present paper illustrate the potentially significant implications of the flux conditions at the lateral boundaries in controlling the evolution of porous flows.

Several simplifications merit further attention in subsequent studies. For example, the model could be extended to account for compressibility of the fluids, as the effects of compressibility may become progressively more important for systems in which the distance between the injection well and the far-field fault is increasingly very large. Other extensions could be to consider some of the three-dimensional dynamics and also some of the two-phase flow effects associated with the immiscibility of water and CO_2 (Pruess *et al.* 2003; Hesse *et al.* 2008), heterogeneity of the rock and dissolution of CO_2 in the formation water and other possible reactive effects (cf. Bear 1988; Pruess *et al.* 2003; Nordbotten & Celia 2006).

Our research was supported by NERC and by BP plc. through the BP Institute.

REFERENCES

BACHU, S. & ADAMS, J. 2003 Sequestration of CO_2 in geological media in response to climate change: capacity of deep saline aquifers to sequester CO_2 in solution. *Energy Convers. Manage.* **44**, 3151–3175.

BARENBLATT, G. I. 1996 *Dimensional Analysis, Self-Similarity and Intermediate Asymptotics*. Cambridge University Press.

BEAR, J. 1988 *Dynamics of Fluids in Porous Media*. Dover.

BICKLE, M., CHADWICK, A., HUPPERT, H. E., HALLWORTH, M. & LYLE, S. 2007 Modelling carbon dioxide accumulation at Sleipner: implications for underground carbon storage. *Earth Planet. Sci. Lett.* **255**, 164–176.

CAVANAGH, A. & RINGROSE, P. 2010 In Salah high-resolution heterogeneous simulations of CO_2 storage. *Search and Discovery*, Article No. 80092.

CLASS, H., EBIGBO, A., HELMIG, R., DAHLE, H. K., NORDBOTTEN, J. M., CELIA, M. A., AUDIGANE, P., DARCIS, M., ENNIS-KING, J., FAN, Y., FLEMISCH, B., GASDA, S. E., JIN, M., KRUG, S., LABREGERE, D., BENI, A. N., PAWAR, R. J., SBAI, A., THOMAS, S. G., TRENTY, L. & WEI, L. 2009 A benchmark study on problems related to CO_2 storage in geologic formations. *Comput. Geosci.* **13**, 409–434.

Farcas, A. & Woods, A. W. 2009 The effect of drainage on the capillary retention of CO_2 in a layered permeable rock. *J. Fluid Mech.* **618**, 349–359.

Gasda, S. E., Nordbotten, J. M. & Celia, M. A. 2009 Vertical equilibrium with sub-scale analytical methods for geological CO_2 sequestration. *Comput. Geosci.* **13**, 469–481.

Hesse, M. A., Orr, F. M. Jr. & Tchelepi, H. A. 2008 Gravity currents with residual trapping. *J. Fluid Mech.* **611**, 35–60.

Hesse, M. A., Tchelepi, H. A. & Orr, F. M. Jr. 2006 Scaling analysis of the migration of CO_2 in aquifers. In *the SPE Annual Technical Conference and Exhibition*, San Antonio, TX.

Huppert, H. E. & Woods, A. W. 1995 Gravity-driven flows in porous layers. *J. Fluid Mech.* **292**, 55–69.

IPCC 2005 *IPCC Special Report on Carbon Dioxide Capture and Storage*. Cambridge University Press.

Juanes, R. E., Spiteri, J., Orr, F. M. & Blunt, M. J. 2006 Impact of relative permeability hysteresis on geological CO_2 storage. *Water Resour. Res.* **42**, W12418.

Lyle, S., Huppert, H. E. & Hallworth, M. 2005 Axisymmetric gravity currents in a porous medium. *J. Fluid Mech.* **543**, 293–302.

Mitchell, V. & Woods, A. W. 2006 Gravity driven flow in confined aquifers. *J. Fluid Mech.* **566**, 345–355.

Neufeld, J. A. & Huppert, H. E. 2009 Modelling carbon dioxide sequestration in layered strata. *J. Fluid Mech.* **625**, 353–370.

Neufeld, J. A., Vella, D. & Huppert, H. E. 2009 The effect of a fissure on storage in a porous medium. *J. Fluid Mech.* **639**, 239–259.

Nordbotten, J. M. & Celia, M. A. 2006 Similarity solutions for fluid injection into confined aquifers. *J. Fluid Mech.* **561**, 307–327.

Nordbotten, J. M., Celia, M. A. & Bachu, S. 2004 Analytical solutions for leakage rates through abandoned wells. *Water Resour. Res.* **40**, W04204.

Nordbotten, J. M., Celia, M. A., Bachu, S. & Dahle, H. K. 2005 Semianalytical solution for CO_2 leakage through an abandoned well. *Environ. Sci. Technol.* **39**, 602–611.

Nordbotten, J. M., Kavetski, D., Celia, M. A. & Bachu, S. 2009 Model for CO_2 leakage including multiple geological layers and multiple leaky wells. *Environ. Sci. Technol.* **43**, 739–749.

Obi, E.-O. I. & Blunt, M. J. 2006 Streamline-based simulation of carbon dioxide storage in a North Sea aquifer. *Water Resour. Res.* **42**, W03414.

Phillips, O. M. 1991 *Flow and Reactions in Permeable Rocks*. Cambridge University Press.

Press, W. H., Teukolsky, S. A., Vetterling, W. T. & Flannery, B. P. 1992 *Numerical Recipes in Fortran 77*. Cambridge University Press.

Pritchard, D. 2007 Gravity currents over fractured substrates in a porous medium. *J. Fluid Mech.* **584**, 415–431.

Pritchard, D., Woods, A. W. & Hogg, A. J. 2001 On the slow draining of a gravity current moving through a layered permeable medium. *J. Fluid Mech.* **444**, 23–47.

Pruess, K., Xu, T., Apps, J. & Garcia, J. 2003 Numerical modeling of aquifer disposal of CO_2. *SPE J.* **8**, 49–60.

Vella, D. & Huppert, H. E. 2006 Gravity currents in a porous medium at an inclined plane. *J. Fluid Mech.* **555**, 353–362.

Woods, A. W. & Farcas, A. 2009 On the leakage of gravity currents advancing through sloping layered permeable rock. *J. Fluid Mech.* **618**, 361–379.

Woods, A. W. & Norris, S. 2010 On the role of caprock and fracture zones in dispersing gas plumes in the subsurface. *Water Resour. Res.* **46**, W08522.